AGU PUBLICATIONS

JGR

Journal of Geophysical Research: Space Physics

RESEARCH ARTICLE
10.1002/2016JA023081

Key Points:
- We propose a new analytical model for the risetime of voltage pulses produced by interplanetary nanodust impacts
- The result agrees with Cassini/RPWS cruise data between Earth and Jupiter
- The nanodust properties follow closely the variations in solar wind drift speed, as expected from dynamics

Correspondence to:
N. Meyer-Vernet,
Nicole.Meyer@obspm.fr

Citation:
Meyer-Vernet, N., M. Moncuquet, K. Issautier, and P. Schippers (2016), Frequency range of dust detection in space with radio and plasma wave receivers: Theory and application to interplanetary nanodust impacts on Cassini, *J. Geophys. Res. Space Physics*, *121*, doi:10.1002/2016JA023081.

Received 17 JUN 2016
Accepted 22 NOV 2016
Accepted article online 7 DEC 2016

Frequency range of dust detection in space with radio and plasma wave receivers: Theory and application to interplanetary nanodust impacts on Cassini

N. Meyer-Vernet[1], M. Moncuquet[1], K. Issautier[1], and P. Schippers[1]

[1]LESIA, Observatoire de Paris, PSL Research University, CNRS, Sorbonne University, UPMC, University Paris Diderot, Sorbonne Paris Cité, Meudon, France

Abstract Wave instruments can detect dust in space via the charges released by impact ionization of fast dust grains. Each hypervelocity dust impact produces an electrostatic pulse whose short risetime is a major property determining the frequency range of detection. We propose a simplified analytical model to calculate this risetime and its variation with grains' mass and photoelectron or ambient plasma density, for pulses in spacecraft potential due to fast interplanetary nanodust impacts. We test these calculations by analyzing the high-frequency receiver data of the radio and plasma wave instrument during the cruise phase of the Cassini mission between Earth and Jupiter. These data confirm the dependence of the risetime on grains' mass and speed and heliocentric distance predicted by our calculations. Furthermore, the data show that the nanodust properties follow closely the fluctuations of the solar wind velocity component perpendicular to the magnetic field, as predicted by dynamics. The calculations can be generalized to microdust detection on other spacecraft and might explain previous observations left uninterpreted. These calculations are also relevant for the design of wave receivers, by determining the optimal frequency range for dust detection on future missions.

1. Introduction

In situ detection of fast-moving dust grains in space with electric antennas coupled to wave receivers (see review by *Meyer-Vernet* [2001]) has three main advantages: first, the collecting area is very large since it can be the whole spacecraft surface, second, the method does not require a specific spacecraft attitude for dust detection, and third, the technique is relatively cheap since it is a by-product of instruments designed for measuring radio and plasma waves as well as ambient electron properties via quasi-thermal noise spectroscopy [*Meyer-Vernet et al.*, 1998]. It is thus complementary to specifically designed dust instruments [e.g., *Auer*, 2001] that yield much more complete grains' characterization when the spacecraft is appropriately pointed.

This dust detection technique was pioneered when the radio [*Warwick et al.*, 1977] and the plasma wave [*Scarf and Gurnett*, 1977] instruments on board the spacecraft Voyager independently detected micrometer-sized grains in the dilute rings of Saturn [*Aubier et al.*, 1983; *Gurnett et al.*, 1983], Uranus [*Meyer-Vernet et al.*, 1986a; *Gurnett et al.*, 1987], and Neptune [*Pedersen et al.*, 1991; *Gurnett et al.*, 1991]. This method was then applied to detect microdust on various spacecraft and environments: near a comet on ISEE 3/ICE [*Gurnett et al.*, 1986; *Meyer-Vernet et al.*, 1986b] and Vega [e.g., *Oberc*, 1994, 1996], in Saturn's E ring with Cassini/radio and plasma wave instrument (RPWS) [e.g., *Kurth et al.*, 2006; *Ye et al.*, 2014a], in the solar wind near 1 AU with STEREO/WAVES [e.g., *Zaslavsky et al.*, 2012; *Belheouane et al.*, 2012], and even in the outer solar system [*Gurnett et al.*, 1997].

The method has been extended to measure fast nanodust in Jovian nanodust streams with Cassini/RPWS [*Meyer-Vernet et al.*, 2009a] and led to the serendipitous discovery on board STEREO at 1 AU of nanodust picked up by the solar wind [*Meyer-Vernet et al.*, 2009b]—a new kind of interplanetary dust that had been predicted by *Mann et al.* [2007]. The pickup of these particles by the solar wind is akin to that of freshly produced ions [*Luhmann*, 2003] and produces their ejection from the inner heliosphere over large distances [*Hamilton et al.*, 1996; *Czechowski and Mann*, 2010].

These interplanetary nanoparticles have been later analyzed in detail using several years of STEREO/WAVES data [*Zaslavsky et al.*, 2012; *Le Chat et al.*, 2013, 2015] but cannot be detected by Wind/WAVES because of

the antenna properties and operating mode [*Meyer-Vernet et al.*, 2014]. Unfortunately, STEREO measurements are limited to about 1 AU heliocentric distance. In contrast, Cassini/RPWS has been able to detect fast interplanetary nanodust during its cruise trajectory between 1 and 5 AU, with a flux compatible with particles originating in the inner solar system and picked up by the solar wind [*Schippers et al.*, 2014, 2015], in agreement with models of dynamics [*Czechowski and Mann*, 2012; *Mann et al.*, 2014]. For example, for particles of mass 5×10^{-21} kg (about 8 nm radius), the average flux at 1 AU measured by Cassini/RPWS was of the order of magnitude of 10^{-1} m^{-2} s^{-1} [*Schippers et al.*, 2014; 2015], similar to the average value measured by STEREO/WAVES [*Meyer-Vernet et al.*, 2009b; *Zaslavsky et al.*, 2012; *Le Chat et al.*, 2013; 2015], with large fluctuations detected on both spacecraft as predicted by models [see, e.g., *Czechowski and Mann*, 2012; *Juhász and Horányi*, 2013].

The mechanism of nanodust detection with Cassini/RPWS in the solar wind is simpler than that responsible for nanodust detection on STEREO, which relies on the variation in electric potential of only one antenna boom whose photoelectron sheath is affected by the impact plasma cloud [*Pantellini et al.*, 2012b, 2013; *Zaslavsky et al.*, 2012]. This STEREO mechanism requires thick antennas with an adequate implantation geometry [*Meyer-Vernet et al.*, 2014, 2015] so that a part of one antenna is exposed to solar radiation and close to the impacted region of the spacecraft—as is the case for the X (Z) antenna on STEREO A (B) [see *Meyer-Vernet et al.*, 2009b, Figure 2]. In contrast, on Cassini the geometry is very different, with electric antennas extending nearly symmetrically far from the spacecraft of rough cylindrical shape and a large high-gain antenna. Hence, on Cassini, nanodust impacts are simply detected via nearly identical voltages measured simultaneously by the three monopole antennas [*Meyer-Vernet et al.*, 2009a; *Schippers et al.*, 2015], revealing pulses in spacecraft potential. This mechanism is similar to that responsible for microdust detection on various spacecraft equipped with electric antennas having a monopole configuration [*Meyer-Vernet*, 2001]. Most impacts take place on the spacecraft surface far from the antennas (of much smaller surface area), and impact ionization produces plasma cloudlets made of dust and spacecraft covers material ejected from the impacted surface. In the absence of dust impacts, a spacecraft in the solar wind is charged positively by photoelectron emission which largely dominates the collection of ambient electrons; therefore, the spacecraft attracts the electrons of the impact-produced cloudlet while repelling the positive ions. The recollection of particles of total charge Q by the spacecraft surface of capacitance C_{SC} produces a potential pulse $\delta V_{SC} \sim Q/C_{SC}$. This produces similar pulses $\delta V \sim -\delta V_{SC}$ detected on each antenna arm connected in monopole mode (so that the wave receiver measures the difference between the antenna's potential and that of the spacecraft), whereas antennas in dipole mode (measuring the difference in potential between two antenna arms) detect a much smaller signal [*Meyer-Vernet et al.*, 1996, 2009a, 2014].

Therefore, upon each dust impact, the monopole antennas detect a potential pulse, whose risetime is determined by the cloudlet's behavior in the spacecraft environment and whose decay time (generally much longer) is determined by the discharge constant of the spacecraft [*Meyer-Vernet*, 1985]. This decay time depends on well-studied spacecraft charging concepts [*Whipple*, 1981; *Garrett*, 1981] and has been discussed in detail for the particular case of microdust impacts on the STEREO spacecraft [*Zaslavsky*, 2015].

In contrast, the pulses' risetime is much more difficult to modelize since it depends on both the impact and ambient plasmas. Contrary to the generally longer decay time, this risetime has not been analyzed previously because it is not large compared to the time resolution of the Cassini/RPWS waveform analyzer [*Gurnett et al.*, 2004], whereas Wind/WAVES [*Bougeret and et al.*, 1995] cannot detect pulses in spacecraft potential, and, as we noted above, STEREO/WAVES [*Bougeret et al.*, 2008] detects nanodust impacts via a different mechanism [see, e.g., *Meyer-Vernet et al.*, 2015].

To the best of our knowledge, the results presented below are the first calculations (section 2) and measurements (section 3) of this essential parameter as a function of grains' mass and heliocentric distance. In section 4, we further show that this time scale closely follows changes in solar wind properties; indeed, our results confirm that the detected interplanetary dust smaller than about 10 nm is moving roughly at the solar wind drift speed (the solar wind velocity component normal to the magnetic field), as predicted by dynamics [*Czechowski and Mann*, 2010, 2012; *Mann et al.*, 2014] for particles of sufficiently small gyroradius to follow the guiding center approximation. We then generalize our calculations of the pulses' risetime to microdust detection on other spacecraft, thereby explaining previous observations left uninterpreted. Finally, we derive some consequences of our results for future wave instruments, in particular Plasma Wave Investigation (PWI) on Bepi-Colombo, RPW on Solar Orbiter, and FIELDS on Solar Probe Plus [*Bale et al.*, 2016], since the pulses' risetime determines the optimal frequency range for dust detection. Unless otherwise stated, units are SI.

2. Risetime of Pulses in Spacecraft Potential for Nanodust Impacts

2.1. The Impact Plasma Cloud

Let us consider a plasma cloudlet produced by impact ionization and assume for simplicity that it contains Q/e positive charges and the same number of negative charges at temperature T_c, is uniform, of half-spherical shape of radius R_c, and expanding at constant speed v_E from the impact region. Impact ionization yields of materials relevant for the STEREO and Cassini spacecraft have been measured recently for microdust impacting at speeds below 40 km/s [*Collette et al.*, 2014], but no useful data from laboratory calibrations or simulations are available for high-speed nanodust. We therefore use an approximation of the empirical relation relating the postimpact free charge Q to the grain's mass m and speed v

$$Q/m \simeq 0.7 v_{(\mathrm{km/s})}^{3.5} \tag{1}$$

based on measurements over a much wider range of speeds [*McBride and McDonnell*, 1999; *Lai et al.*, 2002] than the more recent calibrations and whose extrapolation for fast nanodust is consistent with independent results [*Meyer-Vernet et al.*, 2015]. Beware that in (1), Q/m is in SI units (C/kg), whereas v is in km/s.

Interplanetary nanodust grains of mass $m \lesssim 10^{-20}$ kg (radius $\lesssim$10 nm assuming a mass density of 2.5×10^3 kg m^{-3}) produced in the inner solar system have a gyroradius small enough to be moving at roughly the local solar wind drift speed [*Czechowski and Mann*, 2010, 2012] outward of 1 AU. Under typical solar wind conditions, this yields an average impact speed $v \simeq 300$ km/s at 1 AU [*Czechowski and Mann*, 2010, 2012] (neglecting the much smaller spacecraft speed), which yields from (1) $Q/m \simeq 3.3 \times 10^8$ C/kg, i.e., $Q \simeq 1.6 \times 10^{-12}$C for a typical mass of $m = 5 \times 10^{-21}$ kg (corresponding to a radius of roughly 8 nm). This has major consequences for nanodust detection since from (1), such a nanograin produces a similar impact charge as a grain 10^3-fold more massive moving 5–10 times slower, as is the case for submicron interplanetary and interstellar dust. Since the flux of these larger grains is smaller by many orders of magnitude than the nanodust flux in the interplanetary medium, frequency receivers essentially detect nanodust.

There is much uncertainty on the cloud's temperature and expansion speed. Laboratory measurements and theory yield various and conflicting results, including calculated temperatures of about 1 eV at impact speeds 70–80 km/s [*Hornung and Kissel*, 1994], observed temperatures of a few eV at an impact speed of about 70 km/s [*Krueger and Kissel*, 1984], and in contrast temperatures of 10–60 eV with a weak dependence on impact speed in the range 5–100 km/s [*Ratcliff et al.*, 1997]. Subsequent observations yield 0.9–3 eV for impact speeds varying from 10 to 40 km/s [*Miyachi et al.*, 2008] and recently below 5 eV for electrons at impact speeds below 20 km/s [*Collette et al.*, 2015]. Expansion speeds have been suggested to be of the order of magnitude of the ion thermal speed and to increase with the grain's impact speed, whereas in contrast, *Lee et al.* [2012] measured $v_E \simeq 15$–30 km/s for masses $m > 10^{-17}$ kg impacting at 3–10 km/s, with no evidence of any variation with impact speed.

One can alleviate this lack of robust evidence by deriving an upper limit for the temperature and the expansion speed by using conservation of energy. The kinetic energy of the plasma electrons and ions produced by the impact cannot exceed the kinetic energy $mv^2/2$ of the impacting grain minus the total ionization energy (W_i per ion), whence

$$mv^2/2 \gg (Q/e)\left[3k_B T_c + m_i v_E^2/2 + W_i\right] \tag{2}$$

where T_c is the ion and electron temperature (assumed equal), e is the modulus of the electron charge, and m_i is the typical ion (assumed singly and positively charged) mass. The symbol "$\gg$" comes from the fact that the energy conservation equation neglects various losses as the latent heat of phase transformations and the unknown kinetic energy contribution of the impact-produced neutral particles, which is expected to exceed that of the ionized part since the mass involved in the nanodust impact crater is much greater than that of the ionized particles [*McBride and McDonnell*, 1999]. With an average ion mass $m_i \sim 10 m_p$, $W_i \lesssim 10$ eV, and assuming that the expansion speed is of the order of magnitude of the ion thermal speed at the beginning of the collisionless regime, i.e., $v_E \gtrsim (2k_B T_c/m_i)^{1/2}$, equations (1) and (2) yield $T_c \ll 30$ eV and $v_E \ll 5 \times 10^4$ m/s for $v \simeq 300$ km/s. From these inequalities and the numerical values listed above, we will assume $T_c \sim$ several eV (whose value does not affect significantly our results) and $v_E \sim 10^4$ m/s as order-of-magnitude values.

2.2. Voltage Produced by the Impact Charges

As the cloud's radius R_c increases with time, its average electron number density decreases as $n_c \simeq 3Q/(2\pi e R_c^3)$. The maximum radius R_{max} and lifetime t_{max} of the cloud are reached when its electron density has decreased to the ambient value n, i.e.,

$$R_{max} \sim (3Q/2\pi en)^{1/3} \tag{3}$$

$$t_{max} \sim (3Q/2\pi en)^{1/3}/v_E \tag{4}$$

With $m = 5 \times 10^{-21}$ kg, (3) yields $R_{max} \simeq 1$ m, whence $t_{max} \sim 10^2$ μ s ($\propto d^{2/3}$) for $v_E \simeq 10^4$ m/s and a typical solar wind density $n = 5 \times 10^6$ m^{-3} at $d \simeq 1$ AU.

As a result of expansion, the charged particles become quickly collisionless, and the electrons detach from the (more massive) ions, forming an electron precursor at the edge of the cloud, subjected to an electric field intensity and potential [*Pantellini et al.*, 2012a, 2012b]

$$E_c \lesssim Q/\left(4\pi\epsilon_0 R_c^2\right) \tag{5}$$

$$\Phi_c \lesssim Q/\left(4\pi\epsilon_0 R_c\right) \tag{6}$$

the maximum value corresponding to complete charge separation. The presence of the spacecraft plays a major role via its plasma environment and electric field. The environment depends on the location with respect to the spacecraft-illuminated region—which has a photoelectron sheath—and to the rear side of the spacecraft—which faces a wake partially depleted of protons. However, because of the spacecraft conductive cover, its electric potential Φ_{sc} is uniform, and it is equal to a few times the photoelectron temperature $T_{ph} \simeq 3$ eV in order to recollect a large part of them so that the nonrecollected photoelectrons balance the incoming plasma electron current. This yields $\Phi_{SC} \sim 5-10$ V at 1 AU. This value remains roughly constant between 1 and 5 AU because it depends weakly (logarithmically) on the ratio of the photoelectron flux to the solar wind electron random flux—a quantity which itself varies weakly since the ambient electron density and the photoelectron flux both scale as the inverse-squared heliocentric distance, whereas the ambient electron temperature decreases weakly with distance [*Issautier et al.*, 1999].

The electric field near the spacecraft depends on the relevant length scales, which are mainly determined by the spacecraft size R_{SC} (a few meters) and the Debye lengths of the plasma L_D and of the photoelectrons L_{Dph}. At 1 AU we have $L_D \simeq 10$ m and $L_{Dph} \simeq 1$ m for a typical photoelectron current saturation level of 30 μA m^{-2} yielding a photoelectron number density $n_{ph} \sim 10^8$ m^{-3} in the photoelectron sheath (both Debye lengths increasing roughly in proportion of the heliocentric distance d). This yields a typical electric field of about $E_{SC} \simeq 10$ V/m close to the spacecraft. This field pulls the electrons toward the spacecraft as soon as it exceeds the cloud's field E_c given by (5), i.e., when the cloud's radius and the time exceed

$$R_{c1} \lesssim \left[Q/\left(4\pi\epsilon_0 E_{SC}\right)\right]^{1/2} \tag{7}$$

$$t_{c1} \lesssim R_{c1}/v_E \tag{8}$$

which yields $R_{c1} \lesssim 0.02$ m and $t_{c1} \lesssim 2$ μs for $Q \simeq 1.6 \times 10^{-12}$C at $d = 1$ AU, with $t_{c1} \propto R_{c1} \propto Q^{1/2} d^{1/2}$. Since the cloud's electron thermal speed largely exceeds the expansion speed v_E because $m_i \ll m_e$, approximately half of them are moving toward the spacecraft and recollected in a fraction of μs. The other half is moving outward, and its fraction returning toward the spacecraft depends on its voltage Φ_{SC} compared to the cloud's electron temperature. An important consequence is that the cloud's electron temperature does not affect the number of electrons recollected by more than a factor of 2, which is much smaller than the uncertainty on Q.

One therefore expects a short voltage precursor of time scale smaller than a few μs produced by the motion of the electrons. In planetary environments of temperature smaller than that of the cloud's electrons, a large part of them move faster than the ambient electrons, which may produce a beam-plasma instability and associated wave emission near the ambient plasma frequency, as suggested by *Meyer-Vernet et al.* [2014] and observed in the cold Enceladus plume [*Ye et al.*, 2014b].

2.3. Calculation of the Pulses' Risetime for Positive Spacecraft Potential

The voltage peak is produced by recollection of electrons by the spacecraft, yielding a voltage amplitude $\delta V_{SC} \simeq -Q/C_{SC}$ (neglecting the factor between 0.5 and 1 discussed above). However, the corresponding

risetime of this signal is not the very short time scale of electron recollection, because of the electric potential produced by the cloud's ions. This is because when the electrons are being recollected, the cloud's ions (of typical time scale greater than the electron one by a factor $\sim (m_i/m_e)^{1/2}$) are still very close to the spacecraft and therefore produce on it a signal of similar amplitude and of opposite sign. Indeed, a charge Q at a small distance $\epsilon \ll R_{SC}$ from the surface of a sphere of radius R_{SC} and capacitance C_{SC} induces on it a variation in potential $Q/C_{SC}(1-\epsilon/R_{SC}) \simeq Q/C_{SC}$ [*Jackson*, 1962]. The risetime of the signal is thus roughly the time scale for the voltage produced on the spacecraft by the cloud's positive ions (minus the smaller voltage produced on a monopole antenna [*Meyer-Vernet et al.*, 2014]) to become much smaller than Q/C_{SC}.

This happens when either the cloud envelops the spacecraft or the antennas (of length L), i.e., $R_c > \min(R_{SC}, L)$, or when the ambient electrons or photoelectrons can cancel the voltage produced on the spacecraft by the cloud's positive charge Q. Because of the large value of Q, this screening is nonlinear so that it is not determined by the Debye length and the plasma frequency but requires a more thorough estimate [e.g., *Meyer-Vernet*, 1993]. Indeed, within the photoelectron Debye sheath, the voltage produced on the spacecraft by the impact cloud's positive ions can be canceled by the ambient photoelectrons when enough of them can reach the cloud to shield its charge. Photoelectrons of density n_{ph} and temperature T_{ph} reaching the vicinity of the cloud of radius $R_c = v_E t$ yield a random electron current [*Whipple*, 1981]

$$I_{ph} \simeq -2\pi \left(v_E t\right)^2 e n_{ph} v_{ph} \tag{9}$$

where

$$v_{ph} = \left(eT_{ph(eV)}/2\pi m_e\right)^{1/2} \tag{10}$$

and we have neglected the effect of the attracting potential because $\Phi_c < T_{ph(eV)}$, which holds from (6) for $Q < 4\pi\epsilon_0 T_{ph(eV)}^2/E_{SC} \simeq 10^{-10}$C ($\propto d$) at $d = 1$ AU. The photoelectron charge reaching the cloud thus satisfies $I_{ph} = dq/dt \simeq -At^2$, with $A = 2\pi v_E^2 e n_{ph} v_{ph}$. Hence, the time required for the cloud to collect a charge $-Q$ is $\tau_{ph} \simeq (3Q/A)^{1/3}$, i.e.,

$$\tau_{ph} \simeq \left[3Q/\left(2\pi e n_{ph} v_E^2 v_{ph}\right)\right]^{1/3} = t_{max} \times \left(n/n_{ph}\right)^{1/3} \left(v_E/v_{ph}\right)^{1/3} \tag{11}$$

One therefore expects a pulse's risetime $\tau \simeq \tau_{ph}$ given by (11) if three conditions hold. First, $\tau_{ph} > t_{c1}$ (given by (8)), otherwise the time scale should be calculated by taking into account the cloud's electron collection by the spacecraft simultaneously with the effect of the shielding of the cloud's ion charge by photoelectrons, which requires a detailed simulation outside the scope of this paper.

Second, $\tau_{ph} < t_{c2}$ with

$$t_{c2} = L_{Dph}/v_E \tag{12}$$

for the cloud to be within the photoelectron sheath; otherwise, the cloud's ions are shielded by the ambient electrons rather than by the photoelectrons, as for impacts on spacecraft parts without a photoelectron sheath.

Third, $\tau_{ph} < \tau_d$, where τ_d is the pulses' decay time due to the discharge of the spacecraft, given by $\tau_d \simeq RC_{SC}$ [*Meyer-Vernet*, 1985], where $1/R \simeq dI_{phSC}/d\Phi_{SC}$, the derivative of the spacecraft photoelectron current, which is the fastest charging process in the solar wind. This time scale has been estimated by *Henri et al.* [2011] (equation (11) of that paper) as

$$\tau_d \simeq C_{SC} T_{ph(eV)}/(n e v_e S) \tag{13}$$

where S is the spacecraft surface impacted by the ambient plasma,

$$v_e = \left(eT_{e(eV)}/2\pi m_e\right)^{1/2} \tag{14}$$

T_e being the ambient electron temperature and $\Phi_{SC} < T_{e(eV)}$.

With typical values $n/n_{ph} \sim 1/20$ and $v_{ph} \simeq 2.9\times10^5$ m s^{-1} roughly independent of heliocentric distance, (11) yields a risetime smaller than t_{max} by nearly 1 order of magnitude, equal to $\tau \simeq \tau_{ph} \simeq 12$ μs for $Q \simeq 1.6\times10^{-12}$C at $d = 1$ AU, varying as $Q^{1/3}d^{2/3}$. The time $t_{c2} \simeq 10^2$ μs ($\propto d$) at $d = 1$ AU, so that $\tau < t_{c2}$. The decay time is estimated by substituting $C_{SC} \simeq 200$ pF, $S \simeq 15$ m^2, $T_{ph} \simeq 3$ eV, and $T_e \simeq 10$ eV in (13)–(14), which yields $\tau_d \simeq 94$ μs at 1 AU, varying as $\tau_d \propto d^{2+\gamma/2}$ if the ambient electron density $n \propto r^{-2}$ and temperature $T_e \propto d^{-\gamma}$. Hence, we have $\tau_{ph} \ll \tau_d$.

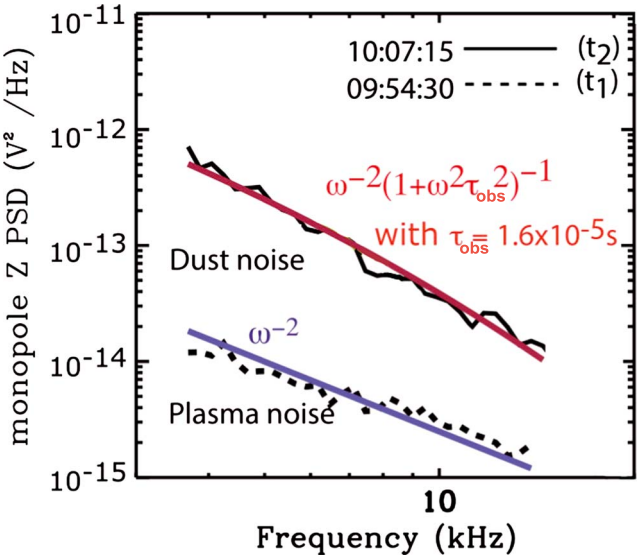

Figure 1. Examples of voltage power spectra measured in monopole mode in the RPWS/HFR lower frequency band, with (continuous line) and without (dotted) nanodust impacts. The curve in red shows the spectrum fitted as explained in section 3.1.

In contrast, if the impact does not take place on a surface having a photoelectron sheath, the risetime is given by replacing in (11) n_{ph} and v_{ph} by the corresponding values for the surrounding electrons, i.e.,

$$\tau_e \simeq \left[3Q/\left(2\pi e n v_E^2 v_e\right)\right]^{1/3} = t_{max} \times \left(v_E/v_e\right)^{1/3} \tag{15}$$

With the parameters considered above, equation (15) yields $\tau_e \simeq 27$ µs for $Q \simeq 1.6 \times 10^{-12}$C at $d = 1$ AU, with $\tau_e \propto Q^{1/3} d^{2/3}$.

Therefore, in both cases (impact plasma cloud within or outside the photoelectron sheath), the risetime is expected to be proportional to the grain's mass raised to the power 1/3 (via Q) and to the heliocentric distance to the power 2/3, with, however, a proportionality factor (cf. equations (11) and (15), respectively), different from the estimate (4) often used in the literature. Since nanodust particles are coming from the inner solar system, most of them are expected to impact on surfaces shielded by photoelectrons; furthermore, we shall see (Figure 2) that the observed risetime is smaller than t_{c2} estimated above (so that the impact cloud is still within the photoelectron sheath); hence, one expects the risetime of interplanetary nanodust produced pulses in spacecraft potential to be given by equation (11), i.e., using (1), to vary with the grain's mass as

$$\tau(m) = b\, m^{1/3} \tag{16}$$

$$b \simeq \left[3(Q/m)/\left(2\pi e n_{ph} v_E^2 v_{ph}\right)\right]^{1/3} \tag{17}$$

which yields $b \simeq 70$ (in SI units) at 1 AU, and varying roughly as $d^{2/3}$.

3. Observed Risetime for Interplanetary Nanodust Impacts on Cassini

Since on Cassini/RPWS, the time resolution of the waveform receiver (WFR) is not small enough to measure accurately the pulse risetime τ, we deduce it from the spectral shape measured by the high-frequency receiver (HFR), which varies roughly as $\omega^{-2}(1 + \omega^2\tau^2)^{-1}$ when the angular frequency ω largely exceeds the inverse of the pulse's decay time [*Meyer-Vernet*, 1985], as is the case for our observations. Therefore, the frequency $(2\pi\tau)^{-1}$ represents a transition between spectral shapes of index close to −4 (for $\omega\tau \gg 1$) and close to −2 (for $\omega\tau \ll 1$). Figure 1 shows an example of the measured voltage power spectrum (continuous line). For comparison, we have superimposed a spectrum acquired a few minutes before the nanodust impacts (dotted), which shows only the f^{-2} shot noise produced by electron impacts and photoelectron emission [*Meyer-Vernet and Perche*, 1989].

3.1. Deducing the Pulses' Risetime as a Function of Mass

The voltage power spectrum produced by a flux mass distribution $F(m)$ of nanodust in the range $m_{\min} < m < m_{\max}$ is, as in *Schippers et al.* [2014],

$$V^2(\omega) \simeq 2S\left[(Q/m)\Gamma/C_{SC}\right]^2 \times \frac{1}{\omega^2}\int_{m_{\min}}^{m_{\max}} dm \left|\frac{dF}{dm}\right| \frac{m^2}{1+\omega^2\tau(m)^2} \tag{18}$$

where Γ is the receiver gain, S the impacted spacecraft surface, and $\tau(m_{\max}) \ll \tau_d$. Note that equation (18) assumes that Q/m is independent of m (in agreement with (1) and as found by most laboratory calibrations) in order to be put outside the integral. This is a reasonable assumption if the grains' speed is roughly independent of mass, which is the case if $m_{\max}$ is smaller than the maximum mass of about 10^{-20} kg which can be accelerated to the solar wind drift speed [*Czechowski and Mann*, 2010; *Mann et al.*, 2014]. Assuming that the grains' mass distribution is given by

$$F = F_0 m^{-\beta} \tag{19}$$

in the range $m_{\min} < m < m_{\max}$, the maximum mass of grains impacting a surface S during the integration time Δt can be estimated from $F(m_{\max})S\Delta t \sim 1/\ln 10$ [*Meyer-Vernet et al.*, 1986a], thus

$$m_{\max} \simeq \left(\ln 10 \times S\Delta t F_0\right)^{1/\beta} \tag{20}$$

In practice, for our data [*Schippers et al.*, 2015], $m_{\max}$ given by (20) is smaller than the maximum mass indicated above, which justifies our assumption that $Q \propto m$ for the detected grains. Note that because the nanodust flux decreases with heliocentric distance d [*Schippers et al.*, 2015], whereas β is positive, the values of $m_{\max}$ given by (20) should decrease as d increases. We shall return to this point later.

In order to test our model (equations (16) and (17)), we now assume that the risetime varies with the grains' mass as

$$\tau(m) \propto m^{\alpha} \tag{21}$$

and we will determine α and the coefficient of proportionality from the data; we will then compare the results to the theoretical values given by (16) and (17). Substituting (19) in (18), and making the change of variables $m = xm_{\max}$, so that from (21) we have $\tau(m) = x^{\alpha}\tau(m_{\max})$, we deduce

$$V^2(\omega) = \frac{A}{\omega^2}\int_{m_{\min}/m_{\max}}^{1} dx \frac{x^{1-\beta}}{1+\omega^2\tau\left(m_{\max}\right)^2 x^{2\alpha}} \tag{22}$$

where

$$A = F_0\beta m_{\max}^{2-\beta} \times 2S\left[(Q/m)\Gamma/C_{SC}\right]^2 \tag{23}$$

For each voltage power spectrum for which $m_{\max}$ is known via equation (20), we determine the risetime τ_{obs} by fitting the function

$$G = g\omega^{-2}(1+\omega^2\tau_{obs}^2)^{-1} \tag{24}$$

to the power spectrum $V^2(\omega)$ observed in the HFR lowest band [*Schippers et al.*, 2014, 2015]. Figure 1 shows an example of such a fitting (in red) with the corresponding value of τ_{obs}.

In practice, we only use the low part of this band, i.e., the frequency range $3.5 < f = \omega/2\pi < f_{\max} \simeq 10$ kHz, in order for the pulses' voltage spectrum to largely exceed the other signals. Comparing (18) and (24), one sees that the fitted value τ_{obs} is an equivalent risetime averaging the actual risetime $\tau(m)$ over the grains' masses m contributing to the power spectrum; it is smaller than $\tau(m_{\max})$ by an amount that depends on the grains' mass distribution and on the frequency range used for the fitting. The relation between τ_{obs} and $\tau(m_{\max})$ can be estimated as follows. When $\omega\tau(m_{\max}) < 1$, one develops the integrand of equation (22) in powers of $\omega^2\tau(m_{\max})^2$ and integrates analytically. Similarly, when $\omega\tau_{obs} < 1$, one develops the function G in powers of $\omega^2\tau_{obs}^2$. Equating the zero-order terms of V^2 and G yields

$$A = g(2-\beta) \tag{25}$$

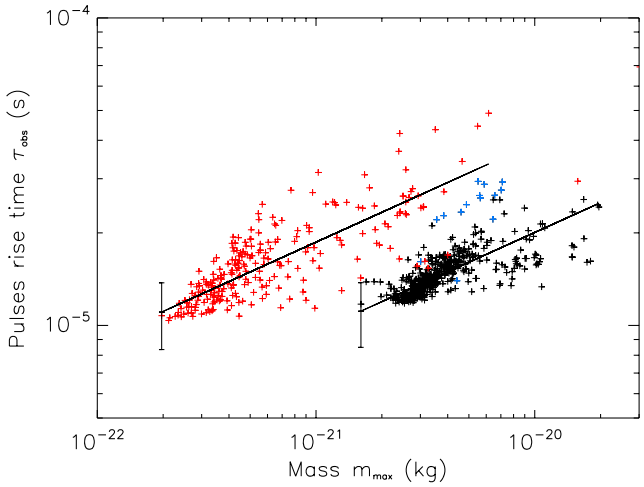

Figure 2. Observed pulse's risetime τ_{obs} versus grain mass m_{max} at 1 AU (black) and 2.9 AU (red) heliocentric distances, and linear log-log best fits, with error bars. The blue crosses are discussed in section 4 and in the appendix.

for $\beta < 2$ and $m_{min}/m_{max} \ll 1$; similarly, equating the first-order terms of V^2 and G yields $\tau(m_{max}) = \tau_{obs}[(2+2\alpha-\beta)g/A]^{1/2}$, in which we substitute g/A from (25) to yield

$$\tau\left(m_{max}\right) \simeq \tau_{obs}\left[\frac{2+2\alpha-\beta}{2-\beta}\right]^{1/2} \tag{26}$$

Let us substitute in (26) $\alpha = 1/3$ (as predicted by equation (16) and to be verified as posteriori), and $\beta = 5/6$, which holds for collisional fragmentation equilibrium [*Dohnanyi*, 1969] and lies on the extrapolation of the submicron grain distribution [*Grün et al.*, 1985]. In this case, equation (26) yields $\tau(m_{max}) \simeq 1.25\tau_{obs}$, holding for $\omega\tau(m_{max}) < 1$, i.e., $2\pi f_{max} b m_{max}^{1/3} < 1$, thus $m_{max} < 1.175 \times 10^{-20}$ kg which includes most of our data. Because collisional equilibrium does not necessarily hold for nanodust, whose dynamics might affect the mass distribution, the exponent β may be different, but the result depends relatively weakly on β since for $\beta < 3/2$, (26) yields $1.15 < \tau(m_{max})/\tau_{obs} < 1.5$. Note that the substitution in equation (26) of $\alpha = 1/3$ (to be verified as posteriori) only affects the absolute values of the risetime deduced from the observations, but not the determination of the index α.

3.2. Observations

The observations studied in this paper are based on the Cassini/RPWS data analyzed by *Schippers et al.* [2014, 2015]. Figure 2 shows the observed risetime τ_{obs} deduced from the fitting of the spectra as explained in section 3.1, versus m_{max} at two heliocentric distances: 1 AU and 2.9 AU. As noted above, the values of m_{max} (derived from (20)) are smaller at 2.9 AU than at 1 AU because the nanodust cumulative flux decreases with both mass and distance [*Schippers et al.*, 2015]. Indeed, the greater the distance or the larger the mass, the smaller the dust cumulative flux and therefore the smaller the maximum mass of grains that can be detected. In other words, if the flux is too small, very large grains are too rare to have a chance to impact the spacecraft during the small integration time.

In order to minimize bias on the risetime, we have used only the spectra of average power frequency index lying between −2.7 (−2.5) and −4 at respectively 1 (2.9) AU. This data selection is expected to eliminate spectra contaminated by the ubiquitous plasma shot noise [*Meyer-Vernet and Perche*, 1989]. The selection has to be more drastic at smaller heliocentric distances for two reasons: first, the plasma shot noise is greater due to the greater plasma density and temperature and second, the value of τ^{-1} is larger (as shown in Figure 2), making the dust spectrum less easily distinguishable from the plasma shot noise in the studied frequency range because, as we already noted, τ^{-1} determines the frequency below which the dust impact contribution has an approximate f^{-2} spectrum (see equation (24)) similar to that of the shot noise. Note that since the data near 1 AU include a significant range of distances (1 – 1.25 AU), we have normalized them to 1 AU by dividing τ_{obs} by the factor $d_{AU}^{2/3}$.

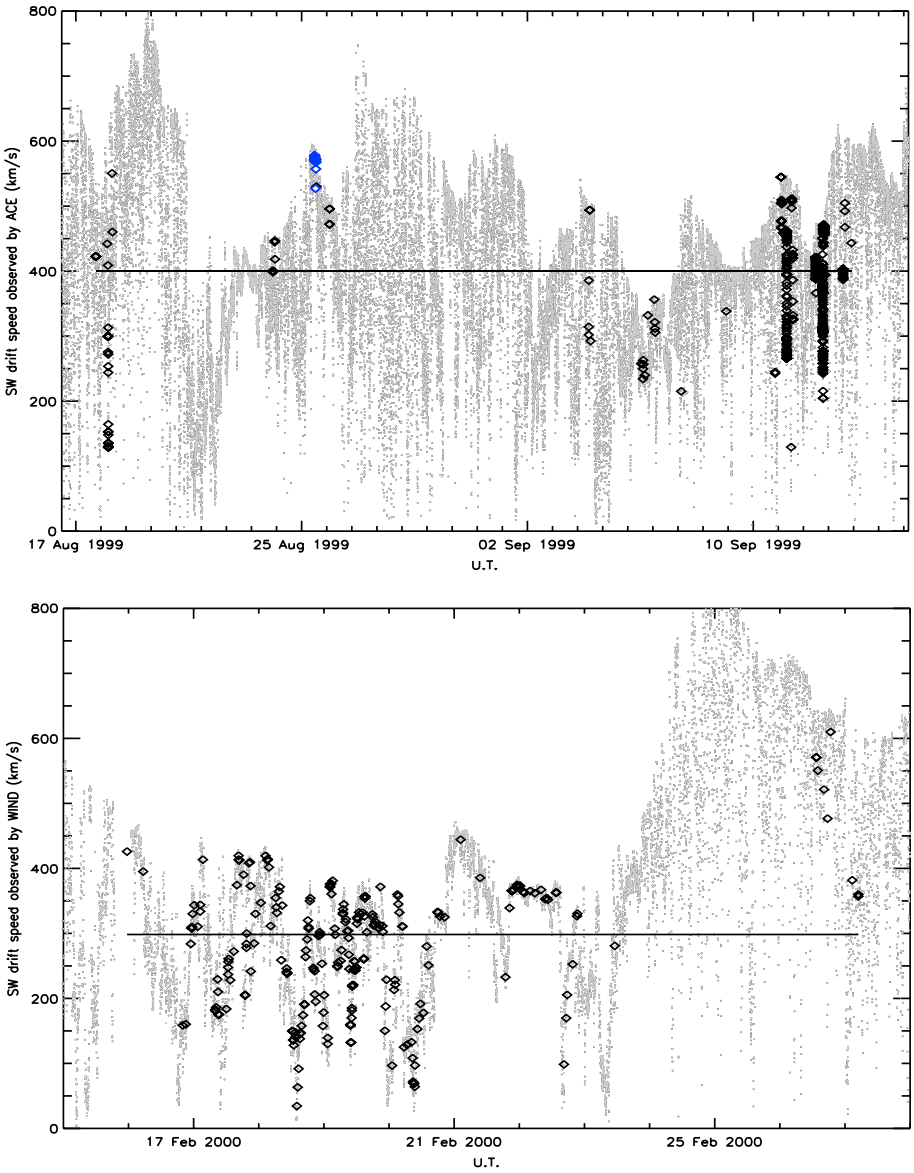

Figure 3. (top) Solar wind drift speed calculated from the solar wind properties observed by ACE (small dots), with the values at the advanced times (see appendix) corresponding to the dust observations by Cassini at 1 AU shown as black diamonds. The horizontal line shows the average (≃400 km/s). The blue dots show the values corresponding to the data in blue in Figure 2 (discussed in section 4 and in the appendix). (bottom) Drift speed calculated from the solar wind properties observed by Wind (small dots), with the values at the advanced times corresponding to the dust observations by Cassini at 2.9 AU shown as black diamonds. The horizontal line shows the average (≃300 km/s).

Fitting these data to a function of the form (21), with a least absolute deviation method [*Press et al.*, 1992], we obtain

$$\tau_{obs} \simeq (55 \pm 2)\, m_{max}^{0.32\pm0.03} \quad \text{for } d \simeq 1 \text{ AU} \tag{27}$$

$$\tau_{obs} \simeq (109 \pm 7)\, m_{max}^{0.32\pm0.05} \quad \text{for } d \simeq 2.9 \text{ AU} \tag{28}$$

It is remarkable that these observed functions both vary with mass with the same power index $\alpha \simeq 0.32$, compatible (within the error bars) with the value 1/3 predicted by equation (16). Consider now the values of b. From equation (17), we have $b \propto [(Q/m)/n_{ph}]^{1/3}$, so that the variation of $n_{ph} \propto d^{-2}$ between 1 and 2.9 AU makes b increase by the factor $2.9^{2/3} \simeq 2$. Let us now consider the grains' speed, which determines Q/m from equation (1). Since the data were acquired in 1999–2000 near solar cycle maximum [*Schippers et al.*, 2015], the solar wind properties are expected to have a large variability; furthermore, the nanodust particles of mass

shown in Figure 2 have a gyrofrequency large enough to make them follow the variable drift speed v_D (the solar wind velocity component perpendicular to the magnetic field) within a time scale on the order of 1 day or less. Hence, we cannot approximate v_D by its value in an average solar wind but must calculate it from the actual solar wind properties, using

$$v_D = \frac{(\mathbf{V}\times\mathbf{B})\times\mathbf{B}}{B^2} = \frac{V}{B}\left(B_\phi^2 + B_z^2\right)^{1/2} \tag{29}$$

where **V** and **B** are the measured solar wind speed and magnetic field and B_ϕ and B_z respectively the azimuthal and vertical components of **B**.

We therefore need the available solar wind data. Since there are no such Cassini measurements available during the nanodust detection periods, we have used data from the ACE and Wind spacecraft for respectively the Cassini observations at 1 and 2.9 AU, taking into account the time delays due to the distance between these spacecraft and Cassini, as explained in Appendix A. Figure 3 shows the drift speed v_D calculated from these solar wind measurements, relevant for the Cassini dust observations at 1 AU (top) and 2.9 AU (bottom). This shows that at the time when the dust data were acquired near 1 AU (black/blue crosses in Figure 2), the average nanodust speed $v \simeq v_D$ was close to 400 km/s (Figure 3, top). On the other hand, at the later time when the dust data were acquired near 2.9 AU (red crosses in Figure 2), the average drift speed v_D at 1 AU was close to 300 km/s (Figure 3, bottom); we deduce the value of v_D at 2.9 AU from the average solar wind speed $V \simeq 400$ km/s (for which $\Omega d/V \simeq d_{\mathrm{AU}}$, where Ω is the solar angular rotation rate), yielding $v_D \simeq 300\times 2^{1/2}\times 2.9/(1+2.9^2)^{1/2} \simeq 400$ km/s, which is similar to the value for the dust data sample at 1 AU. In other words, the temporal variation in solar wind properties measured at 1 AU was such that a similar drift speed of 400 km/s is seen at Cassini when it was at 1 and 2.9 AU (see appendix for details). This yields a similar value of Q/m for the dust data at 1 and 2.9 AU. Equation (17) therefore yields a ratio of intercepts only due to the variation in n_{ph}, i.e., $\simeq 2.9^{2/3} \simeq 2$, which is very close to the observed ratio 109/55 (equations (27) and (28)).

Consider now the absolute values of τ_{obs}. From (26) (with $\alpha = 1/3$ and $\beta = 5/6$), one expects $\tau(m_{\mathrm{max}}) \simeq \tau_{\mathrm{obs}} \times (11/7)^{1/2}$. For nanodust impacting Cassini at 1 AU (respectively 2.9 AU), we expect from equation (17) $b = \tau(m_{\mathrm{max}})/m_{\mathrm{max}}^{1/3} \simeq 70$ (respectively 140) in SI units, whence $\tau_{\mathrm{obs}}/m_{\mathrm{max}}^{1/3} \simeq 70\times(7/11)^{1/2} \simeq 55$ (respectively 110), which lie within the error bars of the observed values given by equations (27) and (28). This agreement confirms our calculations and suggests that the values used for the charge yield (1) and the expansion speed v_E in equation (17) are correct in order of magnitude.

4. Discussion

Even though Figure 2 shows a large dispersion of the data, the variation with mass to the power $\alpha = 1/3$ is determined with a very small uncertainty. This is not surprising since the determination of the index α is independent of the numerical values used; in particular it does not depend on the particle mass distribution index β nor on the yield Q/m. In contrast, the large dispersion in the values of the risetime was expected because of the variation in dust speed due to the variable solar wind properties.

This can be illustrated by considering data acquired during a brief time interval (roughly half an hour), during which the solar wind properties are expected to remain approximately constant (black/blue crosses in Figure 2). These data points acquired near 1 AU follow a $m^{1/3}$ power law, with an intercept larger than the average value at 1 AU by a factor of roughly 1.6. The blue dots in Figure 3 show the solar wind drift speed v_D determined from solar wind data for this period. This yields $v_D \simeq 550$ km/s, which should yield from equations (17) and (1) an intercept larger than the average value at 1 AU by the factor $(550/400)^{3.5/3} \simeq 1.5$, rather close to the observed value (see appendix for more details).

Another part of the data dispersion is expected to stem from the large number of parameters that are badly known or ignored in our simplified model. In particular, the nanodust mass distribution index β may vary with time and heliocentric distance due to the dynamics of the particles in the variable solar wind [*Czechowski and Mann*, 2012; *Juhász and Horányi*, 2013; *Mann et al.*, 2014]; furthermore, the charge yield Q/m and the expansion speed v_E may vary because of the variation in impact geometry and in the nature of the impacted material [*Collette et al.*, 2014].

Let us now examine whether our calculations can apply to other kinds of dust particles and other spacecraft and environments. First, nanodust detection by STEREO/WAVES is outside the scope of this paper since,

as we already noted, that detection does not rely on pulses in spacecraft potential, which are of much smaller amplitude than the potential pulses of the antenna whose photoelectron sheath has been disrupted [*Meyer-Vernet et al.*, 2009b; *Pantellini et al.*, 2012b; *Zaslavsky et al.*, 2012; *Meyer-Vernet and Zaslavsky*, 2012], even though the screening of the impact plasma ions estimated in section 2.3 might play a role [*Pantellini et al.*, 2013].

On the other hand, our calculations are expected to be applicable to the impacts of micro- or submicro-sized dust particles producing voltages pulses in spacecraft potential when this potential is positive, provided that the applicability conditions listed in section 2.3 hold. In this size range, the dust flux (a few particles per day on a typical spacecraft at 1 AU) precludes detection by a frequency receiver (which would require several impacts during the short acquisition time). Consider thus the detection of micro- or submicro-sized dust particles in the solar wind at 1 AU with the STEREO/WAVES time domain sampler [*Bougeret et al.*, 2008].

The analysis of the data has given the fluxes and their variation with time [*Zaslavsky et al.*, 2012; *Belheouane et al.*, 2012; *Malaspina et al.*, 2015], as well as the shape of the pulses [*Zaslavsky*, 2015]. However, the risetime of the pulses, observed to have a distribution peaking around 20 μs with a mean of 31 μs, has not been interpreted, and its large value compared to the μs electron dynamic time scale was unexplained [*Zaslavsky*, 2015]. It may be noted that the statistics of the risetimes on STEREO is complicated by two facts: first, the recorded pulses are biased by the high-amplitude selection employed in the captures [*Zaslavsky et al.*, 2012; *Malaspina et al.*, 2015] and second, contrary to nanodust, these particles are coming from virtually all directions and impact at different speeds on various regions of the spacecraft (depending on whether they are interstellar [*Mann*, 2010a], beta meteoroids [*Mann et al.*, 2010], or in Keplerian orbits), including the wake side where the environment is expected to be very complex. These effects are expected to produce a large dispersion in risetimes making the genuine variation with mass difficult to extract. So let us concentrate on the median and mean observed risetimes and examine whether they can be explained by our calculations.

From the detection voltage range for these STEREO impacts ($\Delta V = 15-150$ mV), the spacecraft capacitance ($C_{SC} \simeq 200$ pF), and the receiver gain ($\Gamma \simeq 0.5$), the detected impact charges lie in the range $Q \simeq \Delta V C_{SC}/\Gamma \simeq 6\times10^{-12} - 6\times10^{-11}$ C [*Zaslavsky et al.*, 2012; *Malaspina et al.*, 2015]. Inserting this range of Q in equation (11) with the values of n_{ph}, v_{ph}, and v_E given above, we find a risetime of 18–39 μs (which verifies the applicability conditions listed in section 2.3). These theoretical values are close to the median and mean observed pulses' risetimes for microdust and submicron dust impacts on STEREO.

5. Concluding Remarks

We have calculated the risetime of voltage pulses produced by dust particle impacts on a positively charged spacecraft and show that the result agrees with data from the Cassini high-frequency receiver when this instrument detected nanodust between 1 and 5 AU. These calculations explain quantitatively the risetime and its variations with the nanograins' mass and the heliocentric distance. The observations also confirm that the nanograins are moving at the solar wind drift speed calculated from solar wind data, as expected in this grains' size range for which the gyroradius is small enough for the particles to follow the guiding center approximation. Especially noticeable is the fact that during a short time interval when the solar wind properties governing the nanodust speed are different from average, the observed pulses' risetime closely follows the theoretical value calculated from these measured solar wind properties.

Our calculations also enable us to interpret the previously unexplained pulses' risetime for the microdust particles impacting the STEREO spacecraft. An important point is that we can explain why the pulse's risetime largely exceeds the short time scale of electron recollection by the spacecraft. This is because when the electrons are recollected, the positive ions (of much longer time scale because of their large mass) are still very close to the spacecraft, so that they produce a voltage of opposite sign to that produced by electron recollection. For the spacecraft voltage to rise to its maximal value, this ion-produced voltage must decrease, which yields a much longer risetime than that due to electron recollection.

Can our results be used for interplanetary dust detection on future missions in the inner heliosphere, in particular on Bepi-Colombo and Solar Orbiter near 0.3 AU and Solar Probe Plus closer to the Sun? An important problem is that the pulses' decay time due to the discharge of the spacecraft varies with heliocentric distance ($\tau_d \propto d^{2+\gamma/2}$ if $T_e \propto d^{-\gamma}$) faster than the risetime ($\tau_{ph} \propto d^{2/3}$). Hence, when the heliocentric distance decreases, the decay time may become shorter than the risetime, thereby decreasing the dust signal. From (11) and (13),

we find $\tau/\tau_d < 1$ at $d = 0.3$ AU if $Q < 0.7 \times 10^{-11}$C, which should enable detection of nanodust and submicron dust if their flux is large enough to produce a power spectrum exceeding that of the plasma shot and quasi-thermal noise.

Consider now the possibility of dust detection with FIELDS on Solar Probe Plus [*Bale et al.*, 2016]. The spacecraft potential is expected to be negative, and the presence of barriers of potential and large secondary electron emission due to the high plasma temperature produces a complex environment [*Ergun et al.*, 2010; *Guillemant et al.*, 2012, 2013]. Because of the large potential barrier near the spacecraft [*Guillemant et al.*, 2012, 2013], the cloud's electrons may be recollected by the spacecraft despite its negative potential. However, near perihelion ($d \simeq 0.05$ AU), we find $\tau/\tau_d > 10$ if $Q > 10^{-12}$C, which may preclude the detection of large grains because of the large charge-to-mass value due to the high expected impact speeds at this distance.

Appendix A: Using ACE or Wind Solar Wind Data

The radio observations of nanodust impacts by Cassini have been acquired episodically during the beginning of the cruise phase [*Schippers et al.*, 2014, 2015] and gathered for the purpose of the present paper in two epochs (epoch 1: 17 August to 14 September 1999 at ~1 AU and epoch 2: 23 February to 2 March 2000 at 2.9 AU). Unfortunately, the Cassini magnetometer data were not available for these epochs, so that we cannot directly access the local solar wind drift speed v_D for our nanodust impact observations.

For this reason we used the satellites ACE or Wind as "sentinels" at 1 AU to figure out the magnetic environment actually experienced downstream by Cassini at our different observation epochs. Note that we used ACE data for epoch 1 and Wind data for epoch 2, to avoid misplaced data gaps. To do so, we have to estimate the transport time of the advected interplanetary magnetic field from ACE (or Wind) to Cassini, taking into account the solar wind variations [*Ashour-Abdalla et al.*, 2008; *Mailyan and Haaland*, 2008].

We proceed iteratively as follows. We first approximate the time delay from the distance between ACE (or Wind for epoch 2) and Cassini, with a typical transport speed at 1 AU (~300 km/s). Note that since our calculation converges quickly (less than 15 iterations), this initial value need not be accurate. This enables us to compute a first advanced time at ACE (or at Wind for epoch 2). We then use the solar wind magnetic field and velocity observed by ACE (or at Wind for epoch 2) at this advanced time to compute a new spiral, new projected velocity on this spiral, and so on, by iteration of this process.

This algorithm is admittedly very simplified. The two epochs considered are close to the maximum of solar cycle 23, with a succession (typically over 2 or 3 days) of slow/fast streams, each defining its own corotating spiral of expansion and including interactions and shocks between them (Corotating Interaction Region (CIR)). Nevertheless, the algorithm converges quickly for each of our observation times at Cassini, mainly because the typical time scale of variation is larger than or of the same order of the estimated time delays. The error on the time delays may be estimated from the iteration method. Typically, for epoch 1 the time delay from ACE to Cassini is about 2 days with an error of less than 1 h, whereas for epoch 2 the delay from Wind to Cassini is about 8 days with an error of less than 6 h, which is largely enough for the purpose of this paper. The resulting advanced times are shown in Figure 3 (diamonds abscissa).

Finally, consider the bunch of dust impacts of high risetime which lasts over half an hour starting on 27 August 1999 14:00 (blue crosses in Figure 2) discussed in section 4. As can be seen in Figure 3, this bunch corresponds to a maximum of the drift speed at roughly 600 km/s, starting on 25 August 1999 at about 8:00 UT and lasting about 4 h on ACE observations. We have plotted in Figure A1 about 4 days of ACE solar wind data around this period. The data show a stable magnetic structure bracketed with two magnetic discontinuities (M1 and M2) and occurring at the trailing interface between a slow dense and a fast dilute plasma stream—a CIR, where we may clearly identify the different magnetic boundaries (black vertical lines), velocity, and density discontinuities, with a compressive layer bracketed by forward (FS) and reverse (RW) shocks in advance of the fastest stream [e.g., *Burlaga*, 1995]. The delay of propagation of the magnetic structure between ACE and Cassini is found to be about 52 h, so that this maximum drift velocity structure reaches Cassini on 27 August at 14:00. This is a clue that the net excursion (8 sigma from the fitted line) of the pulses' risetime could be due to the collection and acceleration of the nanodust in the high drift velocity structure in which the Lorentz force is the more efficient.

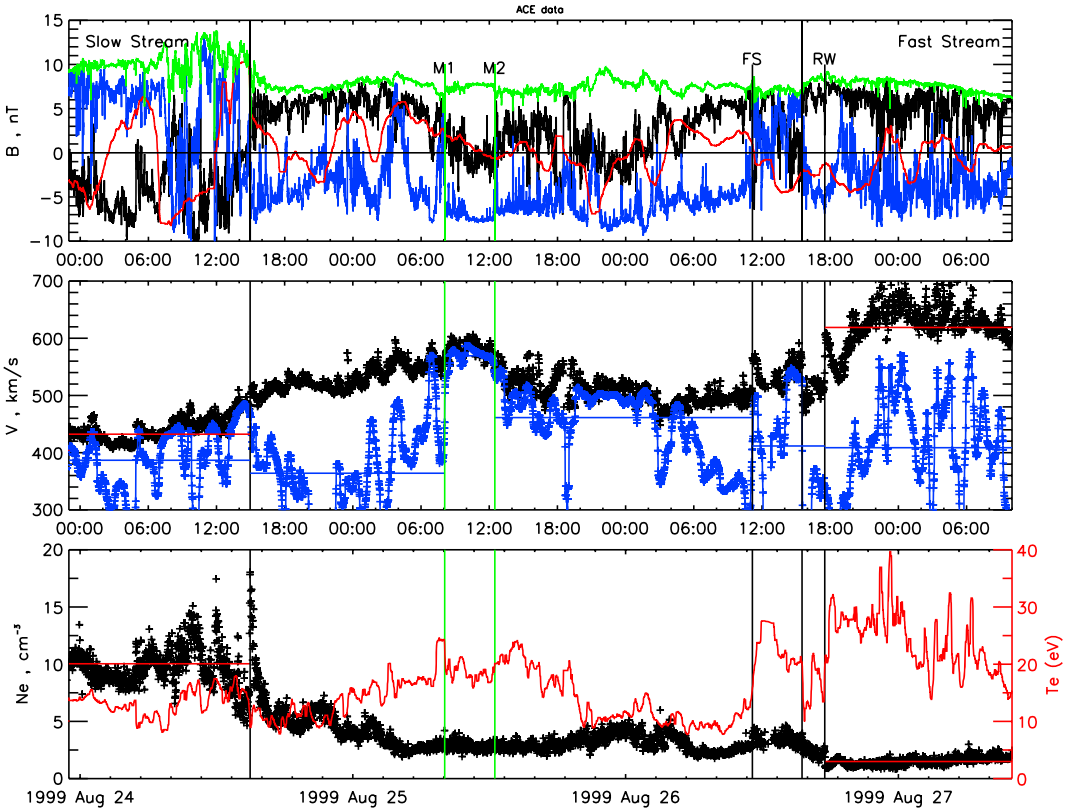

Figure A1. ACE solar wind data (1 min averaged) showing the state of the solar wind during 4 days around the detection of a bunch of particles producing pulses of high risetime. (top) Magnetic field components in GSE coordinates (magnitude in green, B_r in black, B_ϕ in blue, and B_z in red). (middle) Solar wind speed in black and drift speed in blue (with medians as blue horizontal line segments); the red horizontal lines show the median solar wind speeds of the upward and downward periods. (bottom) Electron density (with medians as red horizontal line segments) and temperature.

Acknowledgments
The Cassini/RPWS HF receiver data are available at the University of Iowa or at LESIA (Observatoire de Paris, France) and accessible at www.lesia.obspm.fr/kronos/public_docs.php. We thank the CNES and the CNRS for funding. Data for ACE and Wind are accessible at amda.cdpp.eu/ and were analyzed with the AMDA science analysis system provided by the Centre de Données de la Physique des Plasmas (CDPP) supported by CNRS, CNES, Observatoire de Paris, and Université Paul Sabatier, Toulouse. We thank the ACE SWEPAM and MAG instrument teams as well as the Wind SWE and MFI instrument teams and AMDA for providing their data.

References

Ashour-Abdalla, M., R. J. Walker, V. Peroomian, and M. El-Alaoui (2008), On the importance of accurate solar wind measurements for studying magnetospheric dynamics, *J. Geophys. Res.*, *113*, A08204, doi:10.1029/2007JA012785.

Aubier, M. G., N. Meyer-Vernet, and B. M. Pedersen (1983), Shot noise and particle impacts in Saturn's ring plane, *Geophys. Res. Lett.*, *10*, 5–8.

Auer, S. (2001), Instrumentation, in *Interplanetary Dust*, edited by E. Grün et al., pp. 385–444, Springer, Heidelberg.

Bale, S. D., et al. (2016), The FIELDS instrument suite for Solar Probe Plus, *Space Sci. Rev.*, *204*, 49–82, doi:10.1007/s11214-016-0244-5.

Belheouane, S., A. Zaslavsky, I. Mann, N. Meyer-Vernet, K. Issautier, M. Maksimovic, and V. J. Sterken (2012), Detection of interstellar dust with STEREO/WAVES at 1 AU, *Sol. Phys.*, *281*, 501–506.

Bougeret, J.-L., et al. (1995), WAVES: The radio and plasma wave investigation on the Wind spacecraft, *Space Sci. Rev.*, *71*, 231–263.

Bougeret, J.-L., et al. (2008), The radio and plasma wave investigation on the STEREO mission, *Space Sci. Rev.*, *136*, 487–528.

Burlaga, L. F. (1995), *Interplanetary Magnetohydrodynamics*, Oxford Univ. Press., Oxford.

Collette, A., et al. (2014), Micrometeoroid impact charge yield for common spacecraft materials, *J. Geophys. Res. Space Physics*, *119*, 6019–6026, doi:10.1002/2014JA020042.

Collette, A., et al. (2015), Laboratory investigation of antenna signals from dust impacts on spacecraft, *J. Geophys. Res. Space Physics*, *120*, 5298–5305, doi:10.1002/2015JA021198.

Czechowski, A., and I. Mann (2010), Formation and acceleration of nanodust in the inner heliosphere, *Astrophys. J.*, *714*, 89–99.

Czechowski, A., and I. Mann (2012), *Nanodust in the Solar System: Discoveries and Interpretations (Astrophysics and Space Science Library vol 385)*, edited by I. Mann et al., pp. 47–75, Springer, Heidelberg.

Dohnanyi, J. S. (1969), Collisional model of asteroids and their debris, *J. Geophys. Res.*, *74*, 2531–2554.

Ergun, R. E., et al. (2010), Spacecraft charging and ion wake formation in the near-Sun environment, *Phys. Plasmas*, *17*(072903), doi:10.1063/1.3457484.

Garrett, H. B. (1981), The charging of spacecraft surfaces, *Rev. Geophys. Space Phys.*, *19*, 577–616.

Grün, E. H. A., H. Zook, Fechtig, and R. A. Giese (1985), Collisional balance of the meteoritic complex, *Icarus*, *62*, 244–272.

Guillemant, S., et al. (2012), Solar wind plasma interaction with Solar Probe Plus spacecraft, *Ann. Geophys.*, *30*, 1075–1092.

Guillemant, S. et al. (2013), Simulation study of spacecraft electrostatic sheath changes with the heliocentric distances from 0.044 to 1 AU, *IEEE Trans. Plasma Sci.*, *41*(12), 3338–334.

Gurnett, D. A., E. Grün, D. Gallagher, W. S. Kurth, and F. L. Scarf (1983), Micron-sized particles detected near Saturn by the Voyager plasma wave instrument, *Icarus*, *53*, 236–254.

Gurnett, D. A., T. F. Averkamp, F. L. Scarf, and E. Grün (1986), Dust particles detected near Giacobini-Zinner by the ICE Plasma Wave instrument, *Geophys. Res. Lett.*, *13*, 29–294.
Gurnett, D. A., et al. (1987), Micro-sized particle impacts detected near Uranus by the Voyager 2 Plasma Wave instrument, *J. Geophys. Res.*, *92*, 14,959–14,968.
Gurnett, D. A, W. S. Kurth, L. J. Granroth, and S. C. Allendorf (1991), Micro-sized particles detected near Neptune by the Voyager 2 Plasma Wave instrument, *J. Geophys. Res.*, *96*, 19,177–19,186.
Gurnett, D. A, J. A. Ansher, W. S. Kurth, and L. J. Granroth (1997), Micron-sized dust particles detected in the outer solar system by the Voyager 1 and 2 plasma wave instruments, *Geophys. Res. Lett.*, *24*, 3125–3128.
Gurnett, D. A., et al. (2004), The Cassini radio and plasma wave investigation, *Space Sci. Rev.*, *114*, 395–463.
Hamilton, D. P., E. Grün, and M. Baguhl (1996), Electromagnetic escape of dust from the solar system, in *Physics, Chemistry, and Dynamics of Interplanetary Dust*, vol. 104, edited by B. A. S. Gustafson and M. S. Hanner, pp. 31–34, ASP Conference Series, Kluwer, Dordrecht.
Henri, P., et al. (2011), Observations of Langmuir ponderomotive effects using the Solar TErrestrial RElations Observatory spacecraft as a density probe, *Phys. Plasmas*, *18*(082308).
Hornung, K., and J. Kissel (1994), On shock wave impact ionization of dust particles, *Astron. Astrophys.*, *291*, 324–336.
Issautier, K., N. Meyer-Vernet, M. Moncuquet, and S. Hoang (1999), High-speed solar wind from Ulysses measurements and comparison with heliospheric models, in *Solar Wind Nine, AIP CP-471*, edited by Habbal S. R. et al., pp. 581–584, American Institute of Physics, Woodbury, New York.
Jackson, J. D. (1962), *Classical Electrodynamics*, Wiley, New York.
Juhász, A., and M. Horányi (2013), Dynamics and distribution of nano-dust particles in the inner solar system, *Geophys. Res. Lett.*, *40*, 1–5, doi:10.1002/grl.50535.
Krueger, F. R., and J. Kissel (1984), Experimental investigations on ion emission with dust impact on solid surfaces, in *The Giotto Spacecraft Impact-Induced Plasma Environment. Proceedings Giotto PEWG Meeting, ESA SP-224*, edited by E. Rolfe and B. Battrick, pp. 635–640, ESTEC, Nordwijk.
Kurth, W. S., T. F. Averkamp, D. A. Gurnett, and Z. Wang (2006), Cassini RPWS observations of dust in Saturn's E ring, *Planet. Space Sci.*, *54*, 988–998.
Lai, S. T., E. Murad, and W. J. McNeil (2002), Hazards of hypervelocity impacts on spacecraft, *J. Spacecraft Rockets*, *39*, 106–114.
Le Chat, G., et al. (2013), Interplanetary nanodust detection by the Solar Terrestrial Relations Observatory/WAVES low frequency receiver, *Solar Phys.*, *286*, 549–559.
Le Chat, G., et al. (2015), Effect of the interplanetary medium on nanodust observations by the Solar Terrestrial Relations Observatory, *Sol. Phys.*, *290*, 933–942.
Lee, N., et al. (2012), Measurements of freely-expanding plasma from hypervelocity impacts, *Int. J. Impact Eng.*, *44*, 40–49.
Luhmann, J. G. (2003), Characteristics of scatter-free behavior of heliospheric pick-up ions, *Astrophys. J.*, *592*, 1241–1251.
Mailyan, C. M., and S. Haaland (2008), What is the best method to calculate the solar wind propagation delay?, *Ann. Geophys.*, *26*, 2383–2394.
Malaspina, D. M., et al. (2015), Revisiting STEREO interplanetary and interstellar dust flux and mass estimates, *J. Geophys. Res. Space Physics*, *120*, 6085–6100, doi:10.1002/2015JA021352.
Mann, I., E. Murad, and A. Czechowski (2007), Nanoparticles in the inner solar system, *Planet. Space Sci.*, *55*, 1000–1009.
Mann, I. (2010a), Interstellar dust in the solar system, *Ann. Rev. Astron. Astrophys.*, *48*, 173–203.
Mann, I., A. Czechowski, N. Meyer-Vernet, A. Zaslavsky, and H. Lamy (2010), Dust in the interplanetary medium, *Plasma Phys. Control. Fusion*, *52*(124012).
Mann, I., N. Meyer-Vernet, and A. Czechowski (2014), Dust in the planetary system: Dust interactions in space plasmas of the solar system, *Phys. Rep.*, *536*, 1–39.
McBride, N., and J. A. M. McDonnell (1999), Meteoroid impacts on spacecraft: Sporadics, streams, and the 1999 Leonids, *Planet. Space Sci.*, *47*, 1005–1013.
Meyer-Vernet, N. (1985), Comet Giacobini-Zinner diagnosis from radio measurements, *Adv. Space Res.*, *5*, 37–46.
Meyer-Vernet, N. (2001), Detecting dust grains with electric sensors: Planetary rings, comets, and the interplanetary medium, in *Proceedings of the 7th Spacecraft Charging Technology Conference, ESA SP-476*, edited by R. A. Harris, pp. 635–640, ESTEC, Nordwijk.
Meyer-Vernet, N., M. G. Aubier, and B. M. Pedersen (1986a), Voyager 2 at Uranus: Grain impacts in the ring plane, *Geophys. Res. Lett.*, *13*, 617–620.
Meyer-Vernet, N., et al. (1986b), Plasma diagnosis from thermal noise and limits on dust flux or mass in comet Giacobini-Zinner, *Science*, *232*, 370–374.
Meyer-Vernet, N., and C. Perche (1989), Toolkit for antennae and thermal noise near the plasma frequency, *J. Geophys. Res.*, *94*, 2405–2415.
Meyer-Vernet, N. (1993), Aspects of Debye shielding, *Am. J. Phys.*, *61*, 249–257.
Meyer-Vernet, N., A. Lecacheux, and B. M. Pedersen (1996), Constraints on Saturn's E ring from the Voyager-1 radio astronomy instrument, *Icarus*, *123*, 113–128.
Meyer-Vernet, N., S. Hoang, K. Issautier, M. Maksimovic, R. Manning, M. Moncuquet, and R. Stone (1998), Measuring plasma parameters with thermal noise spectroscopy, in *Measurement Techniques in Space Plasmas: Fields*, vol. 103, edited by R. Pfaff et al., pp. 205–210, Geophys. Monograph Ser., AGU, Washington, D. C.
Meyer-Vernet, N., A. Lecacheux, M. L. Kaiser, and D. A. Gurnett (2009a), Detecting nanoparticles at radio frequencies: Jovian dust stream impacts on Cassini/RPWS, *Geophys. Res. Lett.*, *36*, L03103, doi:10.1029/2008GL036752.
Meyer-Vernet, N., et al. (2009b), Voltage pulses on STEREO/WAVES: Nanoparticles picked-up by the solar wind?, *Sol. Phys.*, *256*, 463–474.
Meyer-Vernet, N., and A. Zaslavsky (2012), In situ detection of interplanetary and Jovian nanodust with radio and plasma wave instruments, in *Nanodust in the Solar System: Discoveries and Interpretations*, edited by I. Mann, N. Meyer-Vernet, and A. Czechowski, pp. 133–160, Springer, Heidelberg.
Meyer-Vernet, N., M. Moncuquet, K. Issautier, and A. Lecacheux (2014), The importance of monopole antennas for dust observations: Why Wind/WAVES does not detect nanodust, *Geophys. Res. Lett.*, *36*(8), 2716–2720, doi:10.1002/2014GL059988.
Meyer-Vernet, N., et al. (2015), The physics and detection of nanodust in the solar system, *Plasma Phys. Control. Fusion*, *57*(014015), doi:10.1088/0741-3335/57/1/014015.
Miyachi, T., et al. (2008), Measurement of temperature after hypervelocity collision of microparticles in the range from 10 to 40 km/s, *Appl. Phys. Lett.*, *93*(174107).
Oberc, P (1994), Dust impacts detected by Voyager-2 at Saturn and Uranus: A post-Halley view, *Icarus*, *211–226*(111).
Oberc, P. (1996), Electric antenna as a dust detector, *Adv. Space Res.*, *17*(12), 105–110.

Pantellini, F., S. Landi, A. Zaslavsky, and N. Meyer-Vernet (2012a), On the unconstrained expansion of a spherical plasma cloud turning collisionless: Case of a cloud generated by a nanometre dust grain impact on an uncharged target in space, *Plasma Phys. Control. Fus.*, *54*, 045005, doi:10.1088/0741-3335/54/4/045005.

Pantellini, F, S. Belheouane, N. Meyer-Vernet, and A. Zaslavsky (2012b), Nano dust impacts on spacecraft and boom antenna charging, *Astrophys. Space Sci.*, *341*, 309–314.

Pantellini, F., G. Le Chat, S. Belheouane, N. Meyer-Vernet, and A. Zaslavsky (2013), On the detection of nano dust using spacecraft based boom antennas, *AIP Conference Proceedings*, *1539*, 414–417.

Pedersen, B. M., et al. (1991), Dust distribution around Neptune: Grain impacts near the ring plane measured by the Voyager Radio Astronomy Experiment, *J. Geophys. Res.*, *96*, 19,187–19,196.

Press, W. H., S. A. Teukolsky, W. T. Vetterling, and B. P. Flannery (1992), *Numerical Recipes*, 2nd edn., Cambridge Univ. Press, New York.

Ratcliff, P. R., et al. (1997), Experimental measurements of hypervelocity impact plasma yield and energetics, *Int. J. Impact Eng.*, *20*, 663–674.

Scarf, F. L., and D. A. Gurnett (1977), A plasma wave investigation for the Voyager mission, *Space Sci. Rev.*, *21*, 289–308.

Schippers, P., et al. (2014), Nanodust detection near 1 AU from spectral analysis of Cassini/Radio and Plasma Wave Science data, *Geophys. Res. Lett.*, *41*, 5382–5388, doi:10.1002/2014GL060566.

Schippers, P., et al. (2015), Nanodust detection between 1 and 5 AU using Cassini wave measurements, *Astrophys. J.*, *806*(77), 1–7, doi:10.1088/0004-637X/806/1/77.

Warwick, J. W., et al. (1977), Planetary and radio astronomy experiment for Voyager missions, *Space Sci. Rev.*, *21*, 309–327.

Whipple, E. C. (1981), Potentials of surfaces in space, *Rep. Prog. Phys.*, *44*, 1197–1250.

Ye, S.-Y., et al. (2014a), Properties of dust particles near Saturn inferred from voltage pulses induced by dust impacts on Cassini spacecraft, *J. Geophys. Res. Space Physics*, *119*, 6294–6312, doi:10.1002/2014JA020024.

Ye, S.-Y., et al. (2014b), Electron density inside Enceladus plume inferred from plasma oscillations excited by dust impacts, *J. Geophys. Res. Space Physics*, *119*, 3373–3380, doi:10.1002/2014JA019861.

Zaslavsky, A. (2015), Floating potential perturbations due to micrometeoroid impacts: Theory and application to S/WAVES data, *J. Geophys. Res. Space Physics*, *120*(2), 855–867, doi:10.1002/2014JA020635.

Zaslavsky, A., et al. (2012), Interplanetary dust detection by radio antennas: Mass calibration and fluxes measured by STEREO/WAVES, *J. Geophys. Res.*, *117*, A05102, doi:10.1029/2011JA017480.